Control Engineering Practice 77 (2018) 41–51

Contents lists available at ScienceDirect

Control Engineering Practice

journal homepage: www.elsevier.com/locate/conengprac

A multirate fractional-order repetitive control for laser-based additive manufacturing

D. Wang, X. Chen *

Department of Mechanical Engineering, University of Connecticut, Storrs, CT, 06269, USA

ARTICLE INFO

Keywords:
Selective laser sintering
Laser scanning mechanism
Numerical simulation
Multirate sampled-data control

ABSTRACT

This paper discusses fractional-order repetitive control (RC) to advance the quality of periodic energy deposition in laser-based additive manufacturing (AM). It addresses an intrinsic RC limitation when the exogenous signal frequency cannot divide the sampling frequency of the sensor, e.g., in imaging-based control of fast laser-material interaction in AM. Three RC designs are proposed to address such fractional-order repetitive processes. In particular, a new multirate RC provides superior performance gains by generating high-gain control exactly at the fundamental and harmonic frequencies of exogenous signals. Experimentation on a galvo laser scanner in AM validates effectiveness of the designs.

1. Introduction

Repetitive control (RC) (Inoue, Nakano, Kubo, Matsumoto, & Baba, 1981) is designed to track/reject periodic exogenous signals in applications with repetitive tasks. By learning from memories of previous iterations in the repetitive task, RC can drastically enhance current control performance in the structured task space. Application examples include tracking controls in magnetic and optical disk drives (Chew & Tomizuka, 1989; Doh, Ryoo, & Chung, 2006), wafer scanners (Chen & Tomizuka, 2014), and robotic manipulators (Cosner, Anwar, & Tomizuka, 1990; Meng, Xie, Liu, Lu, & Ai, 2017), as well as regulation controls in wind turbines (Castro, Salton, Flores, Kinnaert, & Coutinho, 2017; Navalkar et al., 2014), power converters (Nazir, Zhou, Watson, & Wood, 2015), and unmanned aerial vehicles (He, Guo, & Leang, 2017).

This paper studies RC in laser-based additive manufacturing (AM) processes, with a focus on the selective laser sintering (SLS) subcategory. This AM technology applies laser beams as the energy source to melt and join powder materials (Schmidt et al., 2017). A typical workpiece is built from many thousands of thin layers. Within each layer, the laser beam is reflected by mirrors driven by periodic or near-periodic reference signals in a beam deflection mechanism (e.g., a dual-axis galvo scanner) to follow trajectories predefined by the part geometry (in a "slicing" process). This process (see, e.g., Fig. 1) contains highly repetitive thermomechanical interactions (Carter, Martin, Withers, & Attallah, 2014; Kruth et al., 2004; Simchi & Pohl, 2003). As a result, periodic errors are introduced in the laser-material interaction and path planning. Indeed, such periodicity has been validated and leveraged upon to improve control processes in other laser-based AM technologies (Heralić, Christiansson, & Lennartson, 2012; Hoelzle & Barton, 2016; Lim, Hoelzle, & Barton, 2017).

To fully release the capability of RC to fundamentally improve the repetitive laser scanning in SLS AM, the internal model principle (Francis & Wonham, 1975; Hara, Yamamoto, Omata, & Nakano, 1988) must be carefully configured in the control design. In digital RC, an internal model $1/(1 - z^{-N})$ is implemented in the controller, where z is the complex indeterminate in the z-transform and N is the period of the disturbance/reference. N equals the sampling frequency (denoted in this paper as $1/T_s$ or f_s) divided by the fundamental frequency (f_0) of the periodic signal. When N is an integer, the repetitive controller can generate high gains at the fundamental frequency and its harmonics, yielding small gains in the error-rejection dynamics to create the desired servo performances. When f_s is not divisible by f_0, that is, N is not an integer, RC with the rounded N cannot target the aimed harmonic frequencies exactly, resulting in degraded performances.

Several strategies exist to potentially address problems related to fractional-order periods in RC. Steinbuch, Weiland, and Singh (2007) and Ramos and Costa-Castelló (2012) introduce high-order repetitive controllers with delay elements to widen the high-gain regions around the harmonic frequencies. Nakano, She, Mastuo, and Hino (1996), Yao, Tsai, and Yamamoto (2013), and Chen, Yamada, Sakanushi, and Zhao (2013) employ spatial repetitive controllers in a spatial domain to obtain time-invariant disturbance periods. Cao and Ledwich (2002) and Kurniawan, Cao, and Man (2011) propose adaptive RC schemes where

* Corresponding author.
E-mail addresses: dan.wang@uconn.edu (D. Wang), xchen@uconn.edu (X. Chen).

https://doi.org/10.1016/j.conengprac.2018.05.001
Received 31 January 2018; Received in revised form 11 April 2018; Accepted 9 May 2018
Available online 23 May 2018

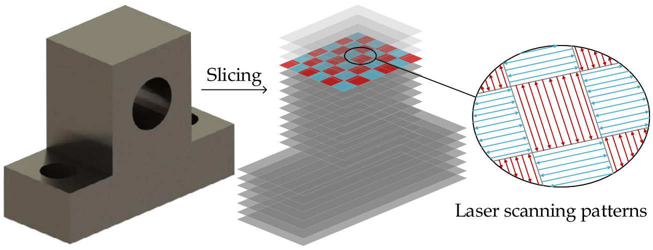

Fig. 1. Schematic of laser scanning patterns in SLS. The example shows the most common "island" pattern in SLS of metallic objects.

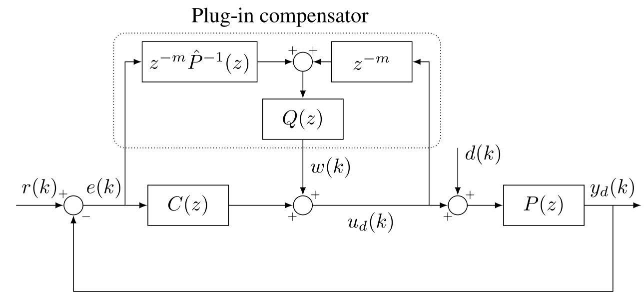

Fig. 2. Block diagram of a plug-in RC design.

the sampling rate is adjusted adaptively to get an integer N. Merry, Kessels, Heemels, Van De Molengraft, and Steinbuch (2011) proposes a delay-varying repetitive controller that uses knowledge of the repetitive variable to continuously adjust the time-varying delay. Nazir et al. (2015), Liu, Zhang, and Zhou (2017), and Zou, Zhou, Wang, and Cheng (2015) design different filters to approximate the fractional orders of delays. Liu, Wang, and Zhou (2016) uses a correction factor to correct the deviated poles of the fractional-order repetitive controller.

Despite the existing literature, it remains not well understood how to create RC *exactly* at the harmonic frequencies in the presence of fractional-order periods and how to systematically analyze the closed-loop performances. To bridge these knowledge gaps, this paper aims at generating enhanced control efforts exactly at desired frequencies in the fractional-order RC. The main result is the development of a multirate RC algorithm and two indirect RC schemes. First, a wide-band RC is achieved by applying the nearest integer of N while widening the attenuation width of each frequency notch in the error-rejection dynamics. In the second indirect RC, a fictitious fundamental frequency is introduced to get an integer N, which creates an overdetermined rejection of the original repetitive errors. The proposed new multirate RC designs the internal model under a second divisible fast sampling frequency f_s' such that $N = f_s'/f_0$ is an integer, and embeds a new zero-phase low-pass filter design to address multirate closed-loop robustness.

Along the course of formulating the multirate RC, an unexpected selective loop-shape modulation is discovered in the intrinsic multirate digital control design. This fundamental behavior, prone to be neglected in the design phase, inspires in the first instance a closed-loop analysis method that exhibits the complete disturbance-attenuation properties of the multirate RC. This analysis method also enables a new design space for applying RC to general systems with mismatched sampling and task periodicity. The remainder of this paper will discuss the theoretical benefits, implementation guidance, and performance comparison of the proposed algorithms. Theoretical analyses are verified by a case study on a galvo scanner in SLS.

A preliminary version of the findings was accepted by the 2018 American Control Conference (Wang & Chen, 2018). This paper substantially extends the research with new theoretical results and illustrative examples. The remainder of this paper is structured as follows. Section 2 reviews a RC design. Two examples in Section 3 elucidate the existence of fractional-order disturbances in SLS. Section 4 builds the proposed fractional-order RC algorithms. Section 5 provides the numerical and experimental verifications of the algorithms. Section 6 concludes the paper.

2. Preliminaries of repetitive control

The proposed fractional-order RC algorithms are based on a plug-in RC design in Fig. 2 (Chen & Tomizuka, 2014). Consider a baseline feedback system composed of the plant $P(z)$ and the baseline controller $C(z)$ (Fig. 2 without the dotted box). $C(z)$ can be designed by means of common servo algorithms, such as PID, H_∞, and lead–lag compensation. The signals $r(k)$, $e(k)$, $d(k)$, and $y_d(k)$ represent, respectively, the reference, the tracking error, the input disturbance, and the system output. Throughout the paper, it is assumed that (1) the coefficients of all transfer functions are real; (2) both $P(z)$ and $C(z)$ are rational, proper, linear, and time-invariant; (3) the baseline feedback loop consisting of $P(z)$ and $C(z)$ is stable.

The plug-in compensator utilizes the internal signals $e(k)$ and $u_d(k)$ to generate a compensation signal $w(k)$. Let m denote the relative degree of $P(z)$, whose nominal model is $\hat{P}(z)$. With the plug-in compensator, the transfer function of the overall controller from $e(k)$ to $u_d(k)$ is

$$C_{all}(z) = \frac{C(z) + z^{-m}\hat{P}^{-1}(z)Q(z)}{1 - z^{-m}Q(z)}. \tag{1}$$

If $Q = (1-\alpha^N)z^{m-N}/(1-\alpha^N z^{-N})$, that is,

$$1 - z^{-m}Q(z) = \frac{1 - z^{-N}}{1 - \alpha^N z^{-N}}, \tag{2}$$

where $\alpha \in [0, 1)$ is a tuning factor that determines the attenuation bandwidth of $1 - z^{-m}Q(z)$, then at the harmonic frequencies ($\omega_k = k2\pi f_0 T_s$, $k \in \mathbb{Z}^+$, the set of positive integers), the magnitude responses of $1 - z^{-m}Q(z)$ are zero because $1 - \mathrm{e}^{-j\omega_k N} = 1 - \mathrm{e}^{-jk2\pi f_0 T_s/(f_0 T_s)} = 1 - \mathrm{e}^{-jk2\pi} = 0$. Hence, $|C_{all}(z)| \to \infty$ and $G_{d\to y_d}(z) = \frac{P(z)[1-z^{-m}Q(z)]}{1+P(z)C(z)} = 0$ when $z = \mathrm{e}^{j\omega_k}$. At the intermediate frequencies, $Q(\mathrm{e}^{j\omega}) \approx 0$, and $|1 - z^{-m}Q(z)|_{z=\mathrm{e}^{j\omega}} \approx 1$ when α is close to 1; thus $C_{all}(z) \approx C(z)$, and the original loop shape is maintained. Choosing a smaller α can yield a wider attenuation bandwidth, at the cost of deviating from the baseline loop shape.

Note that for $Q(z)$ in (2) to be implementable, the disturbance period N should be greater than the relative degree m, which is commonly satisfied in sampled-data regulation control. For instance, in the multirate RC example in Section 5, $N = 40 > m = 3$. Indeed, since the closed-loop bandwidth (B_p) is designed to cover the fundamental disturbance frequency f_0 and B_p is no less than 10% of the Nyquist frequency ($f_s/2$) from principles of feedback design, common control practice thus renders $N = f_s/f_0$ to be greater than 20. That is, N is at least one order of magnitude larger than the relative degree of the plant model under principles of feedback design.

During implementation, zero-phase pairs $q_j(z^{-1})q_j(z)$ ($j \in \mathbb{Z}$) are additionally incorporated into $Q(z)$ for robustness against plant uncertainties at high-frequency regions:

$$Q(z) = \frac{(1-\alpha^N)z^{-(N-m)}}{1-\alpha^N z^{-N}} \prod_{j=0}^{M} q_j(z^{-1})q_j(z), \tag{3}$$

where $M \in \mathbb{Z}$ is determined according to the design requirements. For instance, the following design of $q_i(z)$ ($i \in \mathbb{Z}^+$) places four zeros of $Q(z)$ at $\mathrm{e}^{\pm j\Omega_i T_s'}$ to make its frequency response equal zero at Ω_i:

$$q_i(z) = \frac{1 - 2\cos(\Omega_i T_s)z + z^2}{2 - 2\cos(\Omega_i T_s)}. \tag{4}$$

$$q_0(z) = \frac{(1+z)^{n_0}}{2^{n_0}}, \quad i = 0. \tag{5}$$

Here, $n_0 \in \mathbb{Z}$ is the number of the added zero pairs at the Nyquist frequency. Note that the Q-filter in (3), (4), and (5) is designed assuming an integer N under the sampling time of T_s.

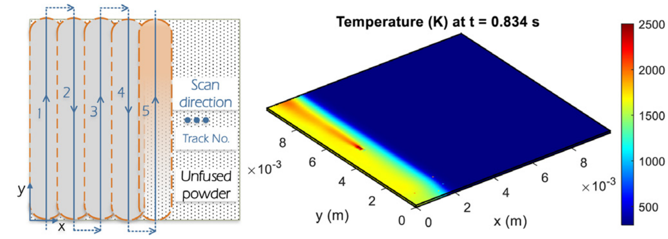

Fig. 3. Schematic of laser path planning and thermal simulation result at $t = 0.834$ s.

3. Fractional-order disturbances in SLS

This section motivates and justifies the application of fractional-order RCs to the field of SLS. The first example, a numerical simulation, shows the periodic thermal cycles during the SLS process and verifies the existence of the fractional-order disturbances. In the second example, fractional-order disturbances are observed to arise from the laser scanning mechanism.

3.1. Periodic thermal cycles in SLS

The SLS is built upon repeated scanning of laser beam on a bed of powder feedstock. The scan trajectories determine the periodicity of the laser-material interactions (see, e.g., Fig. 3). Here, the laser beam melts the powder material following predefined tracks, and monitoring sensors, such as cameras and imaging systems, are applied to obtain the molten pool information. To get a uniform part quality, the molten pool width is desired to be kept at a user-defined reference value (Hofman, Pathiraj, Van Dijk, de Lange, & Meijer, 2012). On the one hand, periodic disturbances are introduced into the SLS process by the complex, repetitive thermomechanical interactions. On the other hand, because vision sensors are restricted in changing sampling rates, the disturbance frequencies, defined by laser path plannings, cannot always divide the sampling frequencies of the monitoring sensors.

To quantitatively demonstrate the periodic thermal cycles, the COMSOL Multiphysics 5.3 software is used to simulate a proof-of-concept benchmark problem. The process parameters, governing equation, initial condition, and boundary conditions used in the simulation are listed in the Appendix. The physics-controlled meshing method is used in the finite element model. The time step T_s is 2 ms, that is, the sampling frequency of the camera is simulated to be $f_s = 1/T_s = 500$ Hz. Eight tracks are sintered bidirectionally with transitions (the left plot of Fig. 3). The right plot of Fig. 3 illustrates the simulation result of the surface temperature distribution of the powder bed at $t = 0.834$ s.

After a short transient, the average molten pool width reaches a steady state as a result of balanced heat influx and diffusion. The molten pool width varies over time and fluctuates around the average value (0.25 mm in the top plot of Fig. 4). In the bidirectional scanning (Fig. 3), when the energy source approaches the end of one track, the large latent heat does not have enough time to dissipate out before the next track starts. This accumulated heat effect results in a higher initial temperature at the beginning of the track to be sintered. Therefore, the molten pool width, directly associated with the initial temperature, generates a periodic increasing spike at the beginning of each track (the top plot of Fig. 4) when the input heat flux keeps constant. Those undesired increasing spikes in the time domain form a periodic disturbance with a repetitive spectrum in the frequency domain (the bottom plot of Fig. 4). The fundamental frequency f_0 of the disturbance is defined by the time taken to scan one single track t_0: $f_0 = 1/t_0 = v/L$, where v is the scan speed and L is the track length. In this example, $f_0 = 100/10 = 10$ Hz, and frequency spikes at $\{nf_0\}$ $(n \in \mathbb{Z}^+)$ appear in the fast Fourier transform (FFT) of the disturbance.

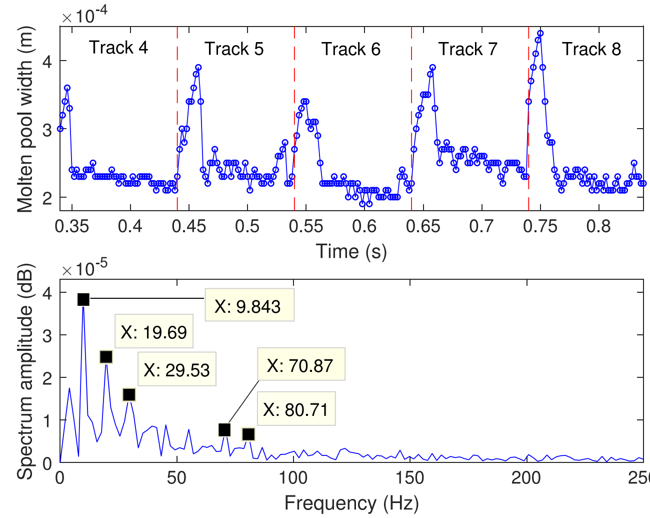

Fig. 4. Simulated example molten pool width in the time domain and the disturbance in the frequency domain.

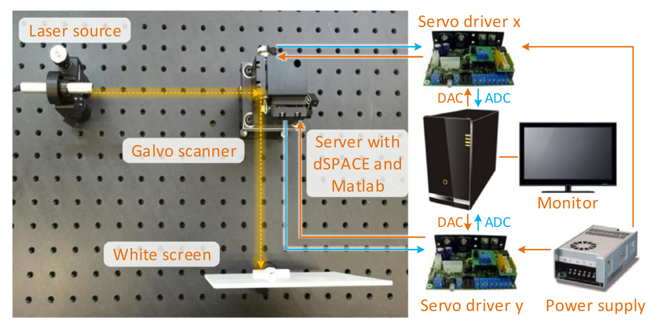

Fig. 5. Schematic of the hardware platform.

In this sample simulation, period $N(= f_s/f_0 = 50)$ is an integer because v/L divides $1/T_s$. However, the scan speed v and the track length L are tailored to the required energy density but not the speed of the monitoring sensors (which is restricted for cameras and general integrated imaging systems). For instance, if $T_s = 3$ ms, $N = 100/3$ will become a non-integer. Therefore, the disturbance periodicity – defined by the scan speed, the part geometry, and the laser path planning – has no guarantees to be an integer multiple of the sampling rate of the molten pool sensors. It is also important to recognize that besides the proof-of-concept bidirectional trajectory, other scanning patterns yield repetitive disturbance components in a similar fashion (see, e.g., experimental results in Dunbar, Denlinger, Gouge, Simpson, and Michaleris (2017). These fractional-order disturbances challenge conventional RC and demand new algorithmic designs for RC to maximize performance in SLS.

3.2. Collaborative control in galvo scanner

A dual-axis galvo scanner in Fig. 5 is a key component in SLS for laser path planning. Typically, the dual-axis galvo scanner consists of two sets of mirrors, motors, and control systems, here referred to as the X channel and the Y channel, respectively. With the collaborative rotation of the two mirrors, the input laser beam is reflected to generate a predefined scanning trajectory at high speed with high precision. The rotation angles of the mirrors are measured by encoders mounted coaxially with the motor shaft in the scanner enclosure.

In practice, periodic disturbances appear in the dual-axis galvo sets. First, examine one single channel (e.g., Y channel) with a simple

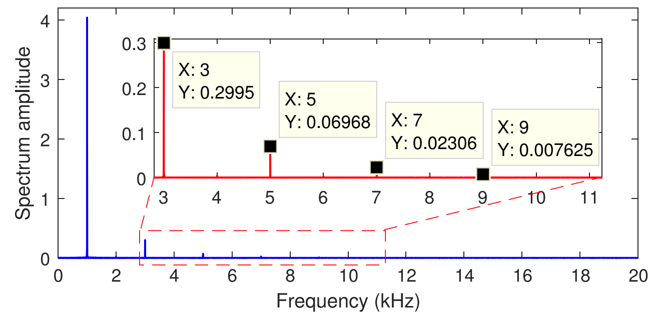

Fig. 6. (Experimental result) FFT of the Y output with a simple harmonic input.

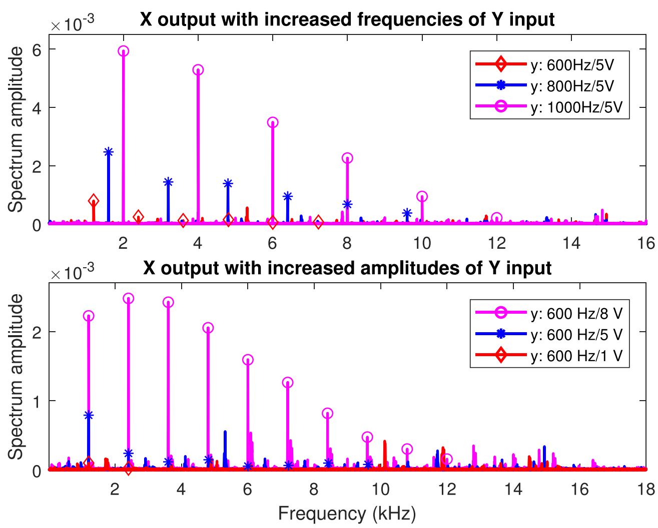

Fig. 7. (Experimental result) FFT of the X output with increased frequencies and amplitudes of Y input.

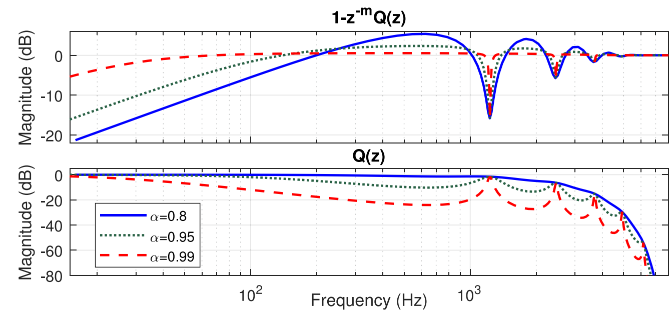

Fig. 8. Magnitude responses of $1 - z^{-m}Q(z)$ and $Q(z)$ in wide-band RC.

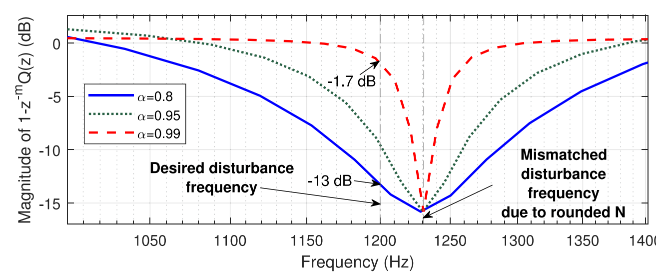

Fig. 9. Zoom-in magnitude responses of $1 - z^{-m}Q(z)$ in Fig. 8.

harmonic signal $A\sin(2\pi f_0 t + \phi)$. Frequency spikes at odd multiples of f_0, instead of a single spike at f_0, show up in the FFT of the channel output (Fig. 6). This is because signal conditioning boards in the servo driver limit the rate of change in the output signal when the slope of the input signal is faster than the predefined slew rate (Jung, 2005). The slewed output waveform is thus not a pure sine waveform and results in harmonics at odd multiples of the fundamental frequency.

Second, the collaborative control of the two channels also introduces periodic disturbances. The mechanical motion of one rotating mirror can transmit to the other mirror as disturbances. In addition, high currents in the ground lines of the two servo drivers can cause the channels to crosstalk (Cambridge Technologies, 2008). When actuating one channel with a simple harmonic signal at f_0, the FFT of the non-actuated channel output was observed to contain a frequency spike at f_0 caused by mechanical vibrations and frequency spikes at $2nf_0$ ($n \in \mathbb{Z}^+$) due to crosstalk. Numerically, if the Y channel is driven with a sine wave at 600 Hz and the X channel has no input, frequency spikes at 1200 Hz, 2400 Hz, 3600 Hz, etc. arise at the FFT of the X output when the crosstalk is unaccounted for. The crosstalk is more obvious with increased amplitudes A and frequencies f_0 of the input signals (Fig. 7).

For both single- and cross-channel disturbances, the disturbance frequencies vary with the input signal frequencies and are not guaranteed to divide the sampling frequency of the galvo scanner. For instance, when $T_s = 1/16$ ms, conventional RC fails in eliminating the crosstalk-induced harmonics at $\{1200i \text{ Hz}\}$ ($i \in \mathbb{Z}^+$) since $N = 16000/1200$ in the internal model is not an integer. Without loss of generality, in this paper, the proposed fractional-order RC algorithms are evaluated on the dual-axis galvo scanner as a case study to reduce the channel crosstalk.

4. Proposed fractional-order RC algorithms

Three algorithms are proposed to tackle a non-integer N in the RC internal model. Two indirect schemes, a wide-band RC and a quasi RC, are first explored. Then the analyses and applications of the main new multirate RC are developed. For concreteness, this section will use the collaborative control example in Sections 3.2 and 5 throughout the discussions and generalize the algorithms along the course of design and analysis.

4.1. Wide-band and quasi repetitive control

The wide-band and quasi RC algorithms are two variants for directly applying the conventional RC in (1) and Fig. 2 to the fractional-order cases. Both of them are implemented at the baseline sampling time, namely, T_s. In the wide-band RC, N is rounded to the nearest integer. Thus, high-control gains are generated near the desired disturbance frequencies. To include these frequencies, the wide-band RC chooses a smaller α to widen the attenuation width of each frequency notch in $1 - z^{-m}Q(z)$, as shown in Fig. 8. With α decreasing from 0.99 to 0.8, the magnitude response of $1 - z^{-m}Q(z)$ in Fig. 9 (a zoom-in view of Fig. 8) decreases from −1.7 dB to −13 dB at 1200 Hz, yielding increased control efforts at the aimed frequencies. Although the wide-band RC cannot perfectly reject the aimed disturbances, attenuation can be achieved to some extent. As the attenuation width increases further, so does the amplification of intermediate frequencies due to the waterbed effect (Bode, 1945).

The proposed quasi RC designs an integer N by introducing a fictitious fundamental frequency that is the greatest common divisor (GCD) of the fundamental and the sampling frequencies, namely, $N = f_s/\text{GCD}(f_s, f_0)$ and $f_0' = \text{GCD}(f_s, f_0) = f_s/N$. In the example from Section 5, with $T_s = 1/16$ ms and $f_0 = 1200$ Hz, $N = 16000/\text{GCD}(16000, 1200) = 40$, and the fictitious fundamental frequency f_0' is $16000/40 = 400$ Hz. Quasi RC designed at $\{400i \text{ Hz}\}$ ($i \in \mathbb{Z}^+$) thus covers the desired harmonics at $\{1200i \text{ Hz}\}$ ($i \in \mathbb{Z}^+$) (with extra servo enhancement at $\{400i \text{ Hz}\}$ ($i, k \in \mathbb{Z}^+$ and $i \neq 3k$)), as shown in Fig. 10. Note that f_0' must be applicable for the quasi RC to work. For an example of $f_0 = 1220$ Hz, $f_0' = \text{GCD}(16000, 1220) = 20$, and the control efforts are

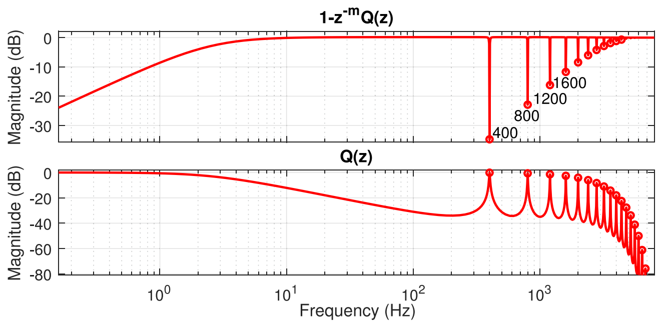

Fig. 10. Magnitude responses of $1 - z^{-m}Q(z)$ and $Q(z)$ in quasi RC.

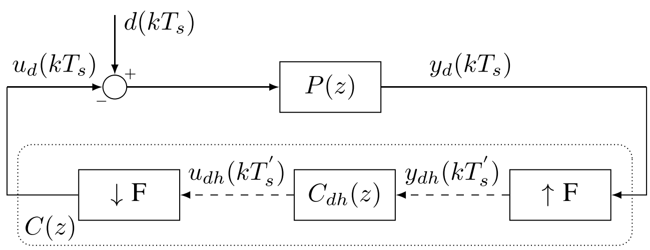

Fig. 11. Block diagram for multirate sampled-data analysis.

largely wasted by generating high gains at many undesired frequencies at $\{20i \text{ Hz}\}$ ($i, k \in \mathbb{Z}^+$ and $i \neq 61k$)).

Inheriting from the plug-in RC design, the stability conditions for the wide-band and quasi RCs are: $\hat{P}^{-1}(z)$, $Q(z)$, and $C(z)$ belong to the set of stable, proper, and rational transfer functions (Chen & Tomizuka, 2013).

The wide-band RC and quasi RC are indirect solutions, only partially attenuating the disturbances. For applications that require stronger servo enhancement, more fundamental structural changes in the controller design will be discussed next.

4.2. Multirate repetitive disturbance attenuation

The proposed multirate RC directly addresses the fractional-order period by introducing a second divisible sampling frequency f_s'. Let f_s' equal the least common multiple (LCM) of the sampling and fundamental frequencies, namely, $f_s' = \mathrm{LCM}(f_s, f_0)$. Without changing the sampling frequency of the plant, the multirate RC algorithm designs the repetitive controller with the internal model under the newly introduced fast sampling frequency. Since $N = f_s'/f_0$ is now an integer, the multirate repetitive controller can thus generate high-gain control signals exactly at the fundamental frequency and its harmonics.

Consider first a multirate sampled-data regulation control in Fig. 11, where the solid and dashed lines represent the slow and fast signals sampled by T_s and $T_s' (\triangleq 1/f_s')$, respectively. T_s' and T_s are related by $T_s' = T_s/F$ ($F > 1$ and $F \in \mathbb{Z}^+$). The main elements here include the plant $P(z)$, the controller $C_{dh}(z)$, the upsampler ↑ F, and the downsampler ↓ F. Based on multirate signal processing (see the Appendix), the frequency response of the equivalent feedback controller $C(z)$ in Fig. 11 is

$$C(e^{j\Omega T_s}) = \frac{1}{F}\sum_{k=0}^{F-1} C_{dh}(e^{j(\Omega T_s' - \frac{2\pi k}{F})}). \tag{6}$$

The proposed multirate RC (Fig. 12) is configured by inserting the upsampling and downsampling blocks into Fig. 2 before and after the all-stabilizing controller.

The transfer functions inside the $C_{all}(z)$ block are implemented at T_s'. With the plug-in RC applied on top of $C_{dh}(z)$, from (6), the frequency

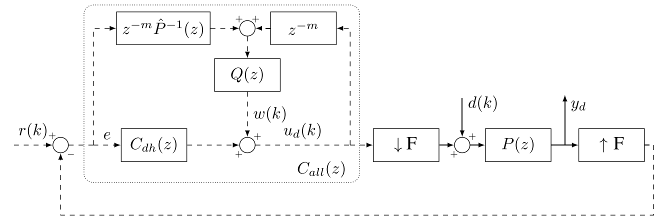

Fig. 12. Block diagram for multirate RC.

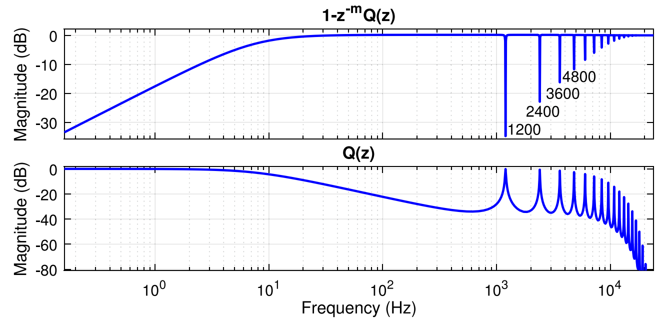

Fig. 13. Magnitude responses of $1 - z^{-m}Q(z)$ and $Q(z)$ in multirate RC.

response of the open-loop transfer function from y_d to the summing junction before $P(z)$ is

$$\tilde{C}(e^{j\Omega T_s}) = \frac{1}{F}\sum_{k=0}^{F-1} C_{all}(e^{j(\Omega T_s' - \frac{2\pi k}{F})}), \tag{7}$$

where

$$C_{all}(e^{j\Omega T_s'}) = \frac{C_{dh}(e^{j\Omega T_s'}) + e^{-jm\Omega T_s'}\hat{P}^{-1}(e^{j\Omega T_s'})Q(e^{j\Omega T_s'})}{1 - e^{-jm\Omega T_s'}Q(e^{j\Omega T_s'})}. \tag{8}$$

Thus, when the reference $r(k)$ is zero (i.e., in regulation problems), block diagram manipulations in Fig. 12 give the Fourier transform of the plant output $y_d(k)$

$$\begin{aligned} Y_d(e^{j\Omega T_s}) &= \frac{P(e^{j\Omega T_s})D(e^{j\Omega T_s})}{1 + \frac{1}{F}P(e^{j\Omega T_s})\sum_{k=0}^{F-1} C_{all}(e^{j(\Omega T_s' - \frac{2\pi k}{F})})} \\ &= \frac{P(e^{j\Omega T_s})D(e^{j\Omega T_s})}{1 + P(e^{j\Omega T_s})\tilde{C}(e^{j\Omega T_s})}. \end{aligned} \tag{9}$$

Before discussing the detailed full multirate closed-loop properties, the authors provide a conceptual example and an overall disturbance-attenuation principle. Consider again $T_s = 1/16$ ms and $f_0 = 1200$ Hz. Multirate RC gives $T_s' = 1/\mathrm{LCM}(16000, 1200) = 1/48$ ms. The plug-in compensator is designed under the sampling time of T_s' such that small gains of $1 - z^{-m}Q(z)$ are generated at the harmonic frequencies of $\Omega_0 = 2\pi n \times 1200$ rad/s ($n \in \mathbb{Z}^+$), as shown in Fig. 13. For disturbances at Ω_0, since the Q-filter design in Section 2 gives $C_{all}(e^{j\Omega_0 T_s'}) \to \infty$, the summation form of C_{all} in (7) also goes to infinity. Thus, in (9), $Y_d(e^{j\Omega_0 T_s}) \to 0$, yielding $y_d(kT_s) = 0$ at Ω_0.

Remark. The proposed algorithm targets exact transformation of the closed loop to formulate an integer parameter of the disturbance period in the internal model, and thereby generates high control gains exactly at the disturbance frequencies. As a trade-off, additional computation is required to facilitate the multirate signal processing. Under certain pairs of disturbance frequency and sampling rate of the system, previous approximate RCs may work more economically under the available computation budget. For instance, when $f_0 = 1199$ Hz and $T_s = 1/16$ ms, then $\mathrm{LCM}(1/T_s, f_0) = \mathrm{LCM}(16000, 1199) = 1918.4$ kHz is orders of magnitude larger than the original sampling rate, resulting in high

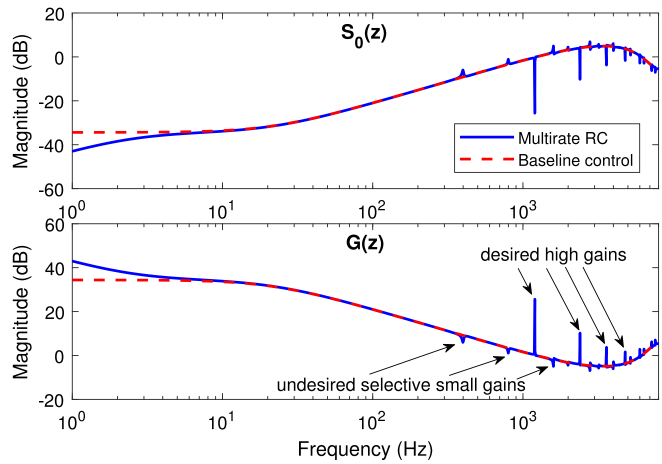

Fig. 14. Frequency responses of $S_0(z)$ and $G(z)$ in Multirate RC with $T_s = 1/16$ ms, $T_s' = 1/48$ ms, $F = 3$, and $f_0 = 1200$ Hz.

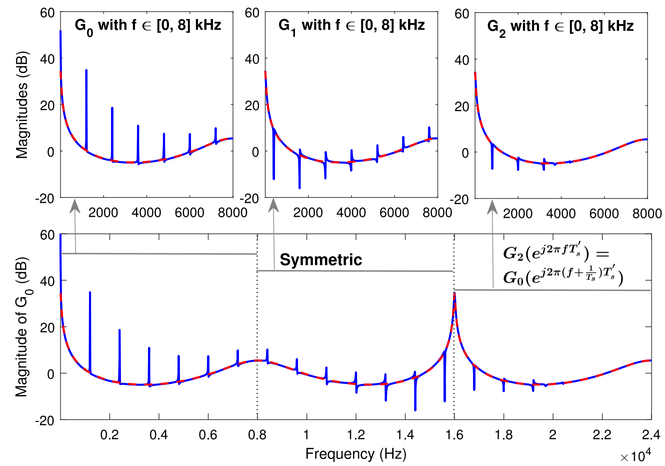

Fig. 15. The relationships between $G_0(e^{j2\pi f T_s'})$, $G_1(e^{j2\pi f T_s'})$, and $G_2(e^{j2\pi f T_s'})$.

computation load that may be cost prohibitive on certain embedded platforms.

Multirate closed-loop analysis

In Fig. 12, the transfer function from the disturbance $d(k)$ to the output $y_d(k)$ equals $S(z) = S_0(z)P(z)$, where $S_0(z)$ is the closed-loop sensitivity function:

$$S_0(e^{j\Omega T_s}) = \frac{1}{G(e^{j\Omega T_s})}, \tag{10}$$

and

$$G(e^{j\Omega T_s}) = 1 + \frac{1}{F} P(e^{j\Omega T_s}) \sum_{k=0}^{F-1} C_{all}(e^{j(\Omega T_s' - \frac{2\pi k}{F})}). \tag{11}$$

To reject disturbances at Ω_0, when the plant dynamics is fixed, $|S_0(e^{j\Omega_0 T_s})|$ in the multirate RC is desired to be small at Ω_0, that is, $|G(e^{j\Omega_0 T_s})| \to \infty$. With the direct Q-filter design under the sampling time of T_s' (Fig. 13), $|S_0(e^{j\Omega T_s})|$ has the desired small gains at the target frequencies, as discussed in the paragraph after (9). However, small spikes also appear in $|S_0(e^{j\Omega T_s})|$, that is, decreasing notches show up in $|G(e^{j\Omega T_s})|$ (Fig. 14). The undesired selective small gains imply potential amplification of other error sources. The complete disturbance-attenuation properties of the proposed multirate RC will be deciphered next to assist in eliminating those error amplifications.

Note that $G(e^{j\Omega T_s})$ in (11) contains hybrid frequency responses of $P(z)$ under the sampling time of T_s and $C_{all}(z)$ under T_s', and the frequency index satisfies the periodicity property:

$$e^{j(\Omega T_s' - \frac{2\pi k}{F})} = e^{j(\Omega - \frac{2\pi k}{T_s})T_s'} = e^{j2\pi(f - \frac{k}{T_s})T_s'}, \tag{12}$$

where $f = \Omega/(2\pi)$ is in Hz. Take the previous example ($T_s = 1/16$ ms, $T_s' = 1/48$ ms, and $F = T_s/T_s' = 3$). Then

$$G(e^{j2\pi f T_s}) = 1 + \frac{1}{3} P(e^{j2\pi f T_s}) \sum_{k=0}^{2} C_{all}(e^{j2\pi(f - \frac{k}{T_s})T_s'}). \tag{13}$$

Let $G_k(e^{j2\pi f T_s'}) = 1 + P(e^{j2\pi f T_s}) C_{all}(e^{j2\pi(f - \frac{k}{T_s})T_s'})$. Then (13) is decomposed to

$$G(e^{j2\pi f T_s}) = \frac{1}{3}\left[G_0(e^{j2\pi f T_s'}) + G_1(e^{j2\pi f T_s'}) + G_2(e^{j2\pi f T_s'})\right]. \tag{14}$$

With $e^{j2\pi f T_s} = e^{j2\pi(f - \frac{k}{T_s})T_s}$, the relationship between G_0 and G_1 is:

$$G_1(e^{j2\pi f T_s'}) = G_0(e^{j2\pi(f - \frac{1}{T_s})T_s'}), \tag{15}$$

and similarly

$$G_2(e^{j2\pi f T_s'}) = G_0(e^{j2\pi(f + \frac{1}{T_s})T_s'}). \tag{16}$$

$G_1(e^{j2\pi f T_s'})$ and $G_2(e^{j2\pi f T_s'})$ are thus shifted versions of $G_0(e^{j2\pi f T_s'})$. Note $S_0(e^{j2\pi f T_s})$ in (10) and $G(e^{j2\pi f T_s})$ in (11) are evaluated from 0 to the slower Nyquist frequency corresponding to T_s, namely, $f \in [0, 8\text{ kHz}]$ in this example. Based on (15), $G_1(e^{j2\pi f T_s'})$ at $f \in [0, 8]$ kHz maps to $G_0(e^{j2\pi f T_s'})$ at $f \in [-16, -8]$ kHz, which is symmetric to $G_0(e^{j2\pi f T_s'})$ at $f \in [8, 16]$ kHz with respect to the line $f = 0$. Similarly, based on (16), $G_2(e^{j2\pi f T_s'})$ with $f \in [0, 8]$ kHz maps to $G_0(e^{j2\pi f T_s'})$ with $f \in [16, 24]$ kHz. Therefore, $G_0(e^{j2\pi f T_s'})$ evaluated at $f \in [0, 24]$ kHz (0 to $0.5/T_s'$, the faster Nyquist frequency corresponding to T_s') includes all the desired information of $G_0(e^{j2\pi f T_s'})$, $G_1(e^{j2\pi f T_s'})$, and $G_2(e^{j2\pi f T_s'})$ under $f \in [0, 8\text{ kHz}]$, as shown in Fig. 15.

It can now be understood that because $G(e^{j2\pi f T_s})$ in (14) is the average of $G_0(e^{j2\pi f T_s'})$, $G_1(e^{j2\pi f T_s'})$, and $G_2(e^{j2\pi f T_s'})$, the undesired small gains of $G(e^{j2\pi f T_s})$ in the bottom plot of Fig. 14 are inherited from $G_1(e^{j2\pi f T_s'})$ and $G_2(e^{j2\pi f T_s'})$ or, equivalently, from $G_0(e^{j2\pi f T_s'})$ at frequencies larger than 8 kHz (Fig. 15).

It will be shown next that the undesired magnitude characteristics of $G_0(e^{j2\pi f T_s'})$ arise from an implicit model mismatch. Recall that

$$G_0(e^{j2\pi f T_s'}) = 1 + P(e^{j2\pi f T_s}) C_{all}(e^{j2\pi f T_s'}). \tag{17}$$

Substituting (8) into (17) gives

$$G_0(e^{j\Omega T_s'}) = \frac{[P(e^{j\Omega T_s})\hat{P}^{-1}(e^{j\Omega T_s'}) - 1]e^{-jm\Omega T_s'}Q(e^{j\Omega T_s'})}{1 - e^{-jm\Omega T_s'}Q(e^{j\Omega T_s'})} + \frac{1 + P(e^{j\Omega T_s})C_{dh}(e^{j\Omega T_s'})}{1 - e^{-jm\Omega T_s'}Q(e^{j\Omega T_s'})}. \tag{18}$$

Fig. 16 presents the frequency responses of $P(e^{j\Omega T_s})$ and $\hat{P}(e^{j\Omega T_s'})$. At low frequencies, $P(e^{j\Omega T_s}) \approx P(e^{j\Omega T_s'}) \approx \hat{P}(e^{j\Omega T_s'})$, and (18) reduces to

$$G_0(e^{j\Omega T_s'}) = \frac{1 + P(e^{j\Omega T_s})C_{dh}(e^{j\Omega T_s'})}{1 - e^{-jm\Omega T_s'}Q(e^{j\Omega T_s'})}. \tag{19}$$

$G_0(e^{j\Omega T_s'})$ thus generates high gains where the magnitude responses of the denominator $1 - z^{-m}Q(z)$ are designed to be small (Fig. 13). At high frequencies, intrinsic model mismatches exist between $P(e^{j\Omega T_s})$ and $\hat{P}(e^{j\Omega T_s'})$ due to different sampling frequencies. Even though the magnitude response of $1 - e^{-jm\omega}Q(e^{j\omega})|_{\omega=\Omega T_s'}$ is small, the first term of (18) must be carefully considered. To eliminate the undesired magnitude shapes, $Q(e^{j\Omega T_s'})$ should be designed small enough at high frequencies to reduce the effect of the model mismatches in $[P(e^{j\Omega T_s})\hat{P}^{-1}(e^{j\Omega T_s'}) - 1]e^{-jm\Omega T_s'}Q(e^{j\Omega T_s'})$.

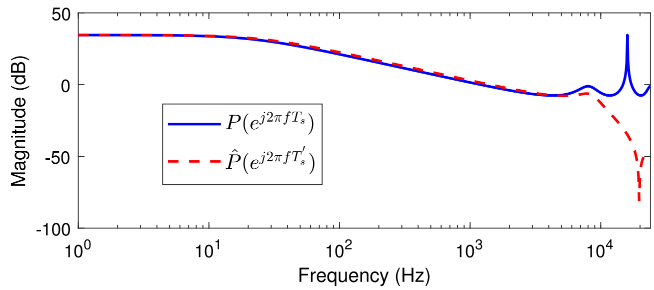

Fig. 16. Magnitude responses of $P(e^{j\Omega T_s})$ and $\hat{P}(e^{j\Omega T_s'})$.

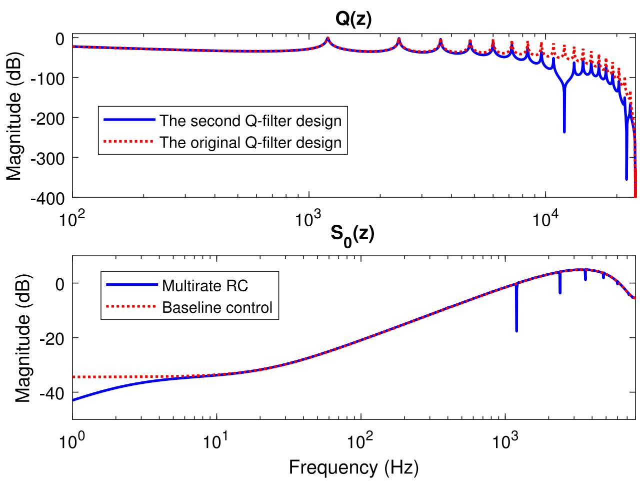

Fig. 17. Magnitude responses of the second Q-filter design.

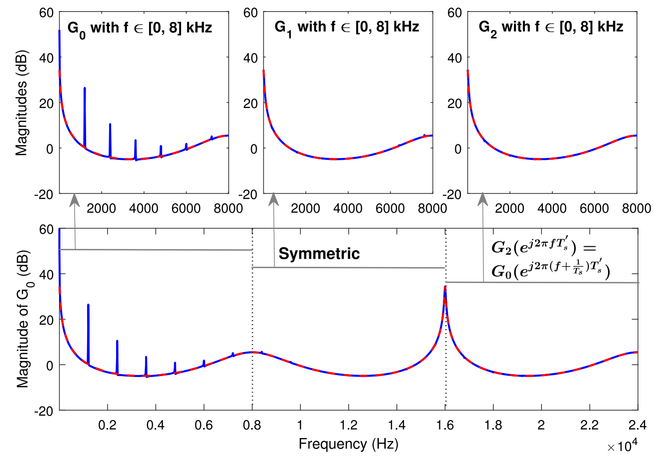

Fig. 18. $G_0(e^{j2\pi fT_s'})$, $G_1(e^{j2\pi fT_s'})$, and $G_2(e^{j2\pi fT_s'})$ of the second Q-filter design.

Compared with the original Q-filter design used in Fig. 14, the multirate RC thus demands an enhanced design with reduced $Q(e^{j\Omega T_s'})$ at high frequencies (the top plot in Fig. 17). This second Q-filter is designed with $\alpha = 0.999$, $n_0 = 2$, $\Omega_1 = 2\pi \times (12\ \text{kHz})$, and $\Omega_2 = 2\pi \times (22\ \text{kHz})$ (see Section 2). As a result, in the multirate RC using the second Q-filter design, the undesired selective small gains of $|G_0(e^{j2\pi fT_s'})|$ disappear (the bottom plot of Fig. 18), which yields a clear magnitude response of the closed-loop sensitivity function with no visible error amplifications, as shown in the bottom plot in Fig. 17.

For more general cases in the multirate RC, the analysis steps are:

1. Given f_s and f_0, identify the second sampling frequency $f_s' = \text{LCM}(f_s, f_0)$ for multirate RC design. Let $F = T_s/T_s' = f_s'/f_s$.
2. Design the repetitive controller in (8) under the deviated sampling frequency to get desired disturbance-attenuation properties.
3. Calculate and plot the closed-loop sensitivity function $S_0(e^{j\Omega T_s})$ and $G(e^{j\Omega T_s})$ in (10) to check if undesired selective small gains show up.
4. Look into $G_k(e^{j2\pi fT_s'})$ ($k = 0, 1, 2, \ldots, F-1$) with $f \in [0, f_s/2]$ to disentangle $G(e^{j\Omega T_s})$ in the summation form. Since all $G_k(e^{j2\pi fT_s'})$'s map into $G_0(e^{j2\pi fT_s'})$, it suffices to analyze $G_0(e^{j2\pi fT_s'})$ under $f \in [0, f_s'/2]$ to identify the frequencies of the undesired notches.
5. Redesign the Q-filter in the repetitive controller, and repeat steps 2–4 to reduce the undesired selective small gains until the design requirements are satisfied.

Stability and robustness

When a stable, bounded model uncertainty $\Delta(z)$ exists such that $\hat{P}(z) = P(z)(1 + \Delta(z))$, standard robust-stability analysis gives that the closed-loop system in the multirate RC is stable if and only if both of the following hold:

1. Nominal stability condition is satisfied, that is, the closed loop is stable when $\Delta(z) = 0$.
2. Robust stability requirement is met by applying the small gain theorem (Doyle, Francis, & Tannenbaum, 2013): for any Ω, $|\Delta(e^{j\Omega T_s})T(e^{j\Omega T_s})| < 1$, where $T(z) = \frac{P(z)C(z)}{1+P(z)C(z)}$ is the complementary sensitivity function.

The second condition translates to $|\Delta(e^{j\Omega T_s})| < 1/|T(e^{j\Omega T_s})|$. Thus, $1/|T(e^{j\Omega T_s})|$ specifies the upper bound of the plant uncertainty at all frequencies. Fig. 19 shows the magnitude responses of $1/T(z)$ from the example in Section 5. Compared with the baseline control (PID control in this example), the introduction of the multirate RC extensively preserves and increases the robust stability bounds, especially at high frequencies. With the multirate RC (solid line in the top plot of Fig. 19), the minimal $1/|T(e^{j\Omega T_s})|$ is -2.9 dB at 1203 Hz, which requires the magnitude response of the uncertainty not to be greater than 71.6% of the magnitude response of the plant at this frequency. Without the lowpass filter $q_0(z^{-1})q_0(z)$ (dash–dot line in the top plot), the minimal $1/|T(e^{j\Omega T_s})|$ of the multirate RC decreases to -10.6 dB (29.5%) at 4801 Hz. Thus, the lowpass filter improves the robustness of the multirate repetitive controller.

The minimal $1/|T(e^{j\Omega T_s})|$ of the wide-band RC (solid line in the bottom plot) is -5.25 dB at 1404 Hz, that is, the uncertainty magnitude at this frequency should be less than 54.6% of the frequency response of the plant. In the quasi RC (dash–dot line in the bottom plot), the upper bound of the plant uncertainties is -2.16 dB (78%) (located at 1203 Hz). The quasi RC is more robust than the wide-band RC, although as shall be discussed in the next section, these two RCs have similar disturbance-attenuation performances.

5. Numerical and experimental verifications in a dual-axis galvo scanner

This section provides implementation guidance and performance comparison of the theoretical analyses. As a case study, the proposed fractional-order RC algorithms are employed to reduce the crosstalk in the collaborative control of the galvo scanner (see Section 3.2).

To attenuate crosstalk-induced disturbances with fractional-order periods in the X channel, the wide-band, quasi, and multirate RC designs in Section 4 are implemented on top of the baseline X-channel controller.

The identified plant model with the sampling time $T_s' = 1/48$ ms is

$$P'(z) = \frac{0.061z^2 + 0.103z + 0.061}{z^5 - 1.485z^4 + 1.032z^3 - 0.433z^2 - 0.057z - 0.061}. \tag{20}$$

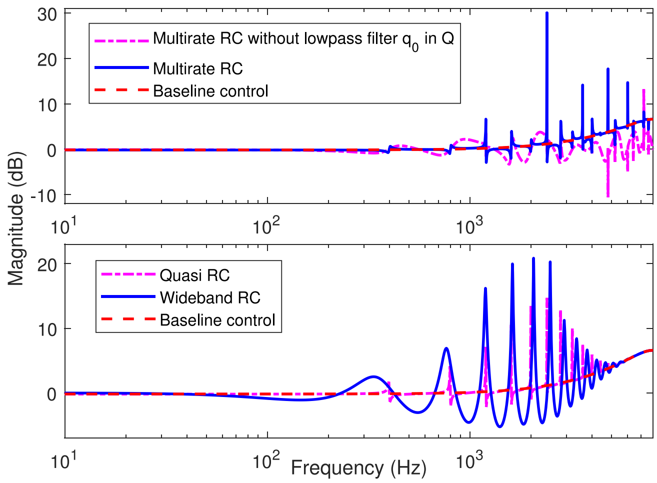

Fig. 19. Magnitude responses of $1/T(z)$, which specify the upper bounds of the plant uncertainties to keep robustness.

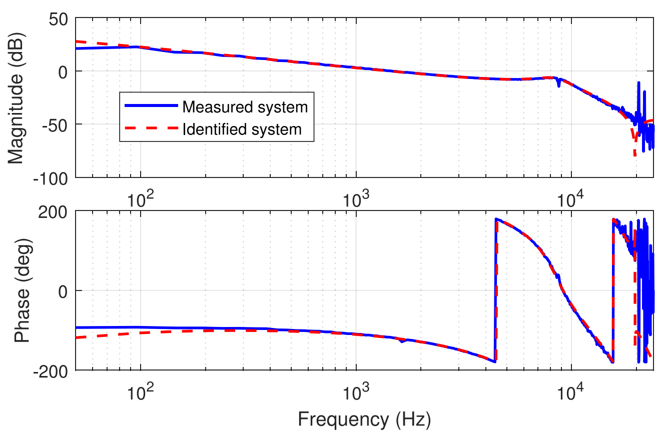

Fig. 20. Bode plot of $P'(z)$ sampled at T'_s.

A stable plant model under the sampling time $T_s = 1/16$ ms is:

$$P(z) = \frac{0.061z^4 + 0.737z^3 + 0.351z^2 + 0.034z + 0.0001}{z^5 + 0.144z^4 - 0.773z^3 - 0.359z^2 - 0.034z - 0.0001}. \tag{21}$$

Fig. 20 shows the frequency responses of the measured and identified $P'(z)$ of the X channel in (20).

The plant models already contain a factory built-in PID-type controller. The baseline feedback loop (Fig. 2 without the plug-in compensator) is thus designed under the sampling time of $T_s = 1/16$ ms by applying $P(z)$ in (21) and by letting $C(z) = 1$ (Wang & Chen, 2017). Such a design provides a 4400 Hz bandwidth in the complementary sensitivity function $T(z)$. Throughout Sections 5.1 and 5.2, n_0 in (5) is chosen to be 3, and M in (3) equals zero.

5.1. Numerical verification

In numerical verification, the same periodic disturbance with five frequency components is introduced into the X-channel loop (Figs. 2 and 12): $d(k) = A\sum_{n=1}^{5} \sin(2\pi n f_0 T_s k)$ with $A = 4$ mV (corresponding to 0.006° of the Y-channel mirror rotation) and $f_0 = 1200$ Hz. As shown in Fig. 21, the position mismatch of the laser hitting the powder bed is $L \tan 2\theta = 1\ \mathrm{m} \times \tan(2 \times 0.006°) \approx 0.21$ mm. When the length of the track to be sintered is 1 mm, this mismatch causes an error of 21%.

The dotted line in Fig. 22 presents the output of the baseline feedback loop in the time domain. Since the PID controller is generic and not tailored to the repetitive disturbance, the baseline controller barely attenuates the frequency spike at 1200 Hz and provides limited attenuation to the other four spikes (the top plot of Fig. 23).

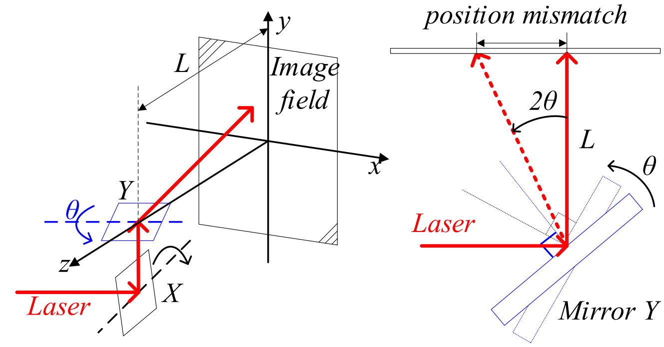

Fig. 21. Schematic diagram of galvo scanner and position mismatch.

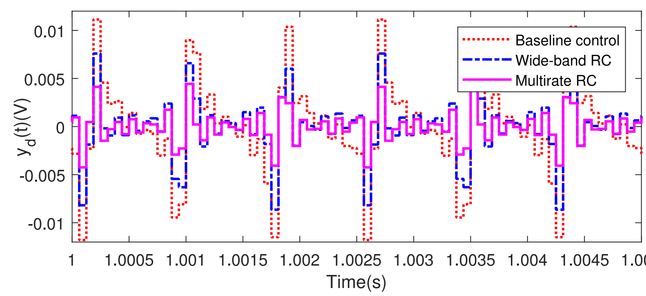

Fig. 22. Plant outputs under baseline control, and the proposed wide-band RC and multirate RC.

The wide-band and quasi RC algorithms are both implemented at the sampling time of $T_s = 1/16$ ms, i.e. $f_s = 16$ kHz. The relative degree of $P(z)$ in (21) is 1, that is, $m = 1$. In the wide-band RC, $N = \mathrm{round}(f_s/f_0) = \mathrm{round}(16000/1200) = 13$. Under this configuration, the frequency spikes the plug-in compensator targets are at $f_s/N = 1230.77$ Hz and its integer multiples. A wider attenuation width is needed in $1 - z^{-m}Q(z)$ to cover the adjacent harmonics at 1200 Hz, 2400 Hz, 3600 Hz, etc. To achieve this goal, α is set as 0.8, as shown in Fig. 8.

In the quasi RC, the fictitious fundamental frequency is configured at 400 Hz such that $N = 16000/400 = 40$. Thus, the plug-in compensator generates high gains at 400 Hz and its integer multiples, covering the target frequencies $\{1200i\ \mathrm{Hz}\}\,(i \in \mathbb{Z}^+)$. α is designed to be 0.999 to achieve good steady-state performance. The time-domain result of the quasi RC is similar to the wide-band RC result shown in the dash–dot line in Fig. 22 and is omitted here. The time-domain outputs show that the wide-band and quasi RCs work better than the baseline control. The frequency-domain analysis in Fig. 23 further shows the first two frequency spikes are remarkably reduced compared with the baseline control. Due to the decreased control effort, the high-frequency spikes at 3600 Hz, 4800 Hz, and 6000 Hz remain largely unchanged.

In the multirate RC, the plug-in compensator is designed at $T'_s = 1/48$ ms ($f'_s = 48$ kHz) with $F = T_s/T'_s = 3$. The relative degree of $P'(z)$ in (20) is 3 ($m = 3$). α is chosen to be 0.999 to reduce the waterbed effect. In this case, $N = f'_s/f_0 = 48000/1200 = 40$. In Fig. 13, small gains of $1 - z^{-m}Q(z)$ are generated exactly at 1200 Hz and its integer multiples. The increased control efforts at high frequencies yield a further-attenuated output in the time domain (the solid line in Fig. 22) and in the frequency domain (the bottom plot of Fig. 23). Besides the attenuated low-frequency spikes, the peaks at 3600 Hz, 4800 Hz, and 6000 Hz are also largely reduced.

The numerical results of the four control systems are compared in Table 1. As a performance metric, for each control system, the 3σ value of the time-domain result is provided, where σ denotes the standard

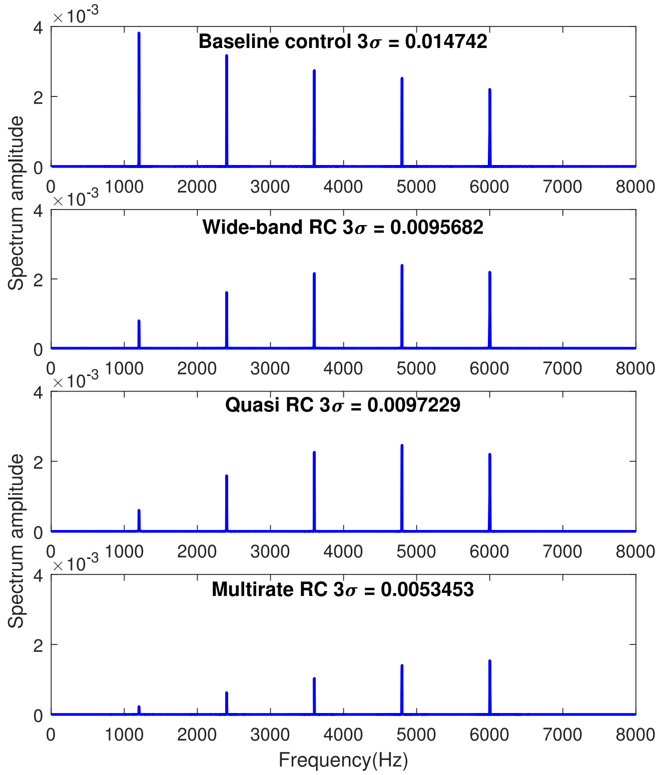

Fig. 23. FFT of plant output sampled at T_s.

Table 1
Numerical and experimental results of the baseline control and the three proposed RC schemes. (N/A denotes “not applicable.”).

		Baseline	Multirate	Wide-band	Quasi
Simulation	3σ	0.0147	0.0053	0.0096	0.0097
	Decreasing	N/A	64%	35%	34%
Experiment	3σ	0.0132	0.0045	0.0074	0.0071
	Decreasing	N/A	66%	44%	46%

deviation. Compared with the baseline control, the application of the multirate, wide-band, and quasi RC algorithms decreases the 3σ values, thereby achieving the desired disturbance-attenuation effect. In more details, the wide-band and quasi RCs have similar performance, and the performance gains are 35% and 34%, respectively. The multirate RC outperforms the other two by reaching a 64% decrease of the 3σ value and reducing the laser point mismatch by one order of magnitude to $0.21 \times (1 - 64\%) \approx 0.075$ mm. In the case of a 1 mm track, the sintering error reduces from 21% to 7%.

5.2. Experimental verification

The control schemes are implemented on a dSPACE DS1104 processor board. Without loss of generality, the Y channel is run with a simple harmonic signal $A\sin(2\pi f_0 t + \phi)$ with $A = 8$ V, $f_0 = 600$ Hz, and $\phi = 0$. The periodic disturbance emerges on the output of the X channel, with frequency spikes at 1200 Hz, 2400 Hz, 3600 Hz, etc. (the top plot in Fig. 24), as stated in Section 3.2. The baseline PID-type controller is unable to reduce the crosstalk between the X and Y channels (the dotted line in Fig. 25).

The experimental and numerical results match well with each other. The output signals $y_d(t)$ in Fig. 25 show the clear performance difference of multirate RC>wide-band RC(≈quasi RC)>baseline control. Indeed, frequency-domain analysis reveals that the wide-band and quasi methods can reduce the first two but not other high-frequency spikes above

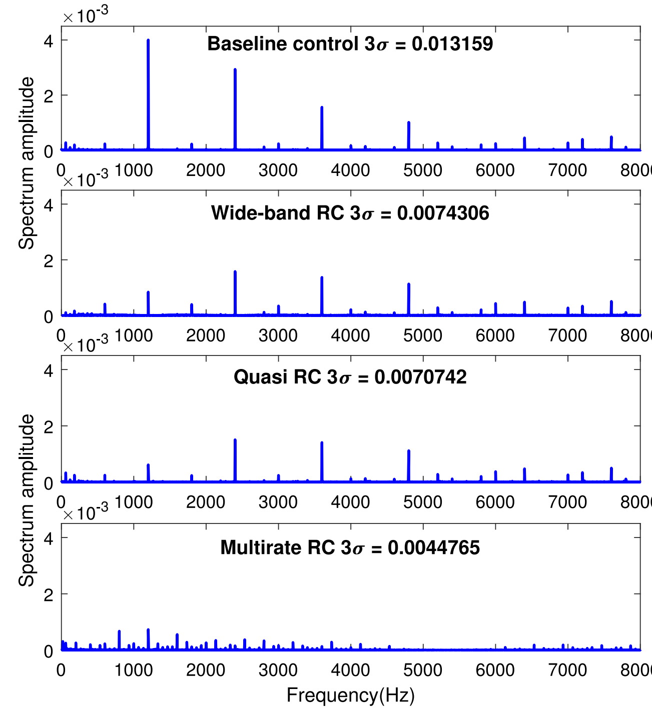

Fig. 24. FFT of plant output sampled at T_s.

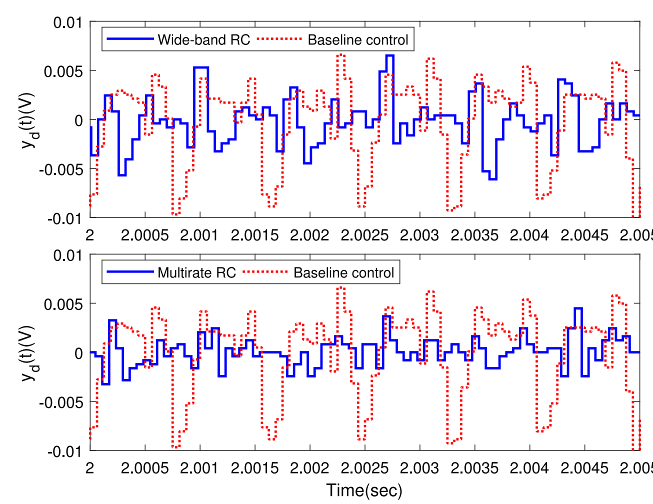

Fig. 25. Plant output of baseline control, and the proposed wide-band RC and multirate RC.

3600 Hz. The multi-rate RC algorithm, on the other hand, can effectively attenuate the periodic frequency spikes appearing at $2nf_0$ ($n \in \mathbb{Z}^+$) by generating frequency notches in $1 - z^{-m}Q(z)$ and enhanced control efforts exactly at those frequencies.

The slight differences between the simulated and experimental results in Table 1 are caused by the different disturbance sources in the two cases. In simulations, the same amplitude is selected for the five introduced frequency spikes. In experiments, the disturbances induced by the crosstalk are different in amplitudes. For each spike, as the frequency increases, the amplitude decreases (Fig. 7).

6. Conclusion

In this paper, three repetitive control (RC) algorithms are proposed to overcome the intrinsic limitation of the RC internal model $1/(1 - z^{-N})$

under fractional-order situations that arise in selective laser sintering additive manufacturing. To apply repetitive error rejection when the fundamental disturbance frequency does not divide the sampling frequency, the wide-band RC scheme widens the attenuation widths to include the desired frequencies of the periodic disturbance. The quasi RC method, on the other hand, creates an integer N by selecting the greatest common divisor of the sampling and fundamental disturbance frequencies as the fictitious fundamental frequency. The multirate RC applies a new fast sampling frequency that allows for exact attenuation at the desired repetitive frequencies. Numerical and experimental results verify the effectiveness of all three algorithms, and the multirate RC algorithm outperforms the wide-band and quasi ones by providing more systematic, precise servo enhancement, particularly at high frequencies.

Acknowledgement

This material is based upon work supported in part by the National Science Foundation under Grant No. 1750027 and by an award from the UTC Institute for Advanced Systems Engineering.

Appendix

Finite element model of SLS

The governing equation for heat flow in SLS is

$$\rho c_p \frac{dT(x,y,z,t)}{dt} = \nabla \cdot (k \nabla T(x,y,z,t)) + q_s, \tag{22}$$

where ρ is the density(kg/m^3) of the material being sintered, c_p is the specific heat (J/(kg·K)), T is the temperature (K), t is the time (s), k is the thermal conductivity (W/(m·K)), and q_s is the rate of local internal energy generated per unit volume (W/m^3) (Kannatey-Asibu Jr, 2009). ρ, c_p, and k are assumed to be temperature-dependent (see Table 5.3 in Arce (2012)).

The initial condition is specified as $T(x,y,z,0) = T_0$, where T_0 is the initial temperature. The timescale of sintering one layer is orders of magnitude faster than the heat transfer in the building (z) direction. The bottom is thus assumed to have no heat loss, and one boundary condition is $-k\frac{\partial T}{\partial z}\Big|_{z=-h} = 0$, where h is the height of the powder bed.

Considering surface conduction, convection and radiation, another boundary condition (Foroozmehr, Badrossamay, Foroozmehr, et al., 2016; Labudovic, Hu, & Kovacevic, 2003; Peyre, Aubry, Fabbro, Neveu, & Longuet, 2008) is applied:

$$-k\frac{\partial T}{\partial z}\Big|_{z=0} = -Q + h_c(T - T_a) + \varepsilon\sigma(T^4 - T_a^4), \tag{23}$$

where ε is the powder bed emissivity, σ is the Stefan–Boltzmann constant, h_c is the convection heat transfer coefficient, T_a is the ambient temperature, and Q is the input heat flux (assuming a Gaussian laser beam profile):

$$Q \approx \frac{2P}{\pi R^2} e^{-\frac{2r^2}{R^2}}, \tag{24}$$

where P is the laser power, R denotes the effective laser beam radius, and r is the radial distance from the center of the laser spot (Labudovic et al., 2003). The process parameters used in Section 3.1 are shown in Table 2.

Proof of (6)

The downsampling operation in Fig. 11 gives

$$U_d(e^{j\Omega T_s}) = \frac{1}{F}\sum_{k=0}^{F-1} U_{dh}(e^{j(\Omega T_s' - \frac{2\pi k}{F})}). \tag{25}$$

From the upsampling operation, the Fourier transforms of y_d and y_{dh} are related by

$$Y_d(e^{j\Omega T_s}) = Y_{dh}(e^{j\Omega T_s'}). \tag{26}$$

Table 2
Parameters for numerical simulation of laser-based AM.

Dimensions of powder bed	10 mm × 10 mm × 100 μm
Powder material	Ti–6Al–4V
Laser power	30 W
Scan speed	100 mm/s
Laser spot diameter	35 μm
Emissivity	0.35
Ambient and initial temperature	23 °C
Convection heat transfer coefficient	12.7 W/(m^2·K)

Note that

$$C(e^{j\Omega T_s}) = \frac{U_d(e^{j\Omega T_s})}{Y_d(e^{j\Omega T_s})},\ C_{dh}(e^{j\Omega T_s'}) = \frac{U_{dh}(e^{j\Omega T_s'})}{Y_{dh}(e^{j\Omega T_s'})}, \tag{27}$$

and thus

$$\sum_{k=0}^{F-1} C_{dh}(e^{j(\Omega T_s' - \frac{2\pi k}{F})}) = \sum_{k=0}^{F-1} \frac{U_{dh}(e^{j(\Omega T_s' - \frac{2\pi k}{F})})}{Y_{dh}(e^{j(\Omega T_s' - \frac{2\pi k}{F})})}. \tag{28}$$

The denominators of the terms on the right side of (28) satisfy

$$\begin{aligned} Y_{dh}(e^{j(\Omega T_s' - \frac{2\pi k}{F})}) &= Y_{dh}(e^{j(\Omega - \frac{2\pi k}{T_s})T_s'}) \\ = Y_d(e^{j(\Omega - \frac{2\pi k}{T_s})T_s}) &= Y_d(e^{j\Omega T_s}), \end{aligned} \tag{29}$$

where the second equal sign is due to the upsampling of (26). Substituting (29) and (25) into (28) gives

$$\begin{aligned} \sum_{k=0}^{F-1} C_{dh}(e^{j(\Omega T_s' - \frac{2\pi k}{F})}) &= \frac{\sum_{k=0}^{F-1} U_{dh}(e^{j(\Omega T_s' - \frac{2\pi k}{F})})}{Y_d(e^{j\Omega T_s})} \\ &= \frac{F U_d(e^{j\Omega T_s})}{Y_d(e^{j\Omega T_s})}. \end{aligned} \tag{30}$$

Hence, according to (27),

$$\sum_{k=0}^{F-1} C_{dh}(e^{j(\Omega T_s' - \frac{2\pi k}{F})}) = F C(e^{j\Omega T_s}), \tag{31}$$

which is equivalent to (6).

References

Arce, A. N. (2012). *Thermal modeling and simulation of electron beam melting for rapid prototyping on Ti-6Al-4V alloys*. North Carolina State University.
Bode, H. W. (1945). *Network analysis and feedback amplifier design*. Princeton, NJ, USA: Van Nostrand.
Cambridge Technologies, I. (2008). *MicroMax 671 series broad level single axis driver electronics*.
Cao, Z., & Ledwich, G. F. (2002). Adaptive repetitive control to track variable periodic signals with fixed sampling rate. *IEEE/ASME Transactions on Mechatronics*, *7*(3), 378–384.
Carter, L. N., Martin, C., Withers, P. J., & Attallah, M. M. (2014). The influence of the laser scan strategy on grain structure and cracking behaviour in SLM powder-bed fabricated nickel superalloy. *Journal of Alloys and Compounds*, *615*, 338–347.
Castro, R. S., Salton, A. T., Flores, J. V., Kinnaert, M., & Coutinho, D. F. (2017). Variable frequency resonant controller for load reduction in wind turbines. *Control Engineering Practice*, *66*, 76–88.
Chen, X., & Tomizuka, M. (2013). Control methodologies for precision positioning systems. In Proceedings of American control conference (pp. 3710–3717). http://dx.doi.org/10.1109/ACC.2013.6580403.
Chen, X., & Tomizuka, M. (2014). New repetitive control with improved steady-state performance and accelerated transient. *IEEE Transactions on Control Systems Technology*, *22*(2), 664–675. http://dx.doi.org/10.1109/TCST.2013.2253102.
Chen, Z., Yamada, K., Sakanushi, T., & Zhao, Y. (2013). Linear matrix inequality-based repetitive controller design for linear systems with time-varying uncertainties to reject position-dependent disturbances. *International Journal of Innovative Computing, Information and Control*, *9*(8), 3241–3256.
Chew, K. K., & Tomizuka, M. (1989). Digital control of repetitive errors in disk drive systems. In *American control conference, 1989* (pp. 540–548). IEEE.
Cosner, C., Anwar, G., & Tomizuka, M. (1990). Plug in repetitive control for industrial robotic manipulators. In *Robotics and automation, 1990. Proceedings, 1990 IEEE international conference on* (pp. 1970–1975). IEEE.

Doh, T.-Y., Ryoo, J., & Chung, M. (2006). Design of a repetitive controller: An application to the track-following servo system of optical disk drives. *IEE Proceedings-Control Theory and Applications*, *153*(3), 323–330.

Doyle, J. C., Francis, B. A., & Tannenbaum, A. R. (2013). *Feedback control theory*. Courier Corporation.

Dunbar, A. J., Denlinger, E. R., Gouge, M. F., Simpson, T. W., & Michaleris, P. (2017). Comparisons of laser powder bed fusion additive manufacturing builds through experimental in situ distortion and temperature measurements. *Additive Manufacturing*, *15*, 57–65.

Foroozmehr, A., Badrossamay, M., Foroozmehr, E., et al. (2016). Finite element simulation of selective laser melting process considering optical penetration depth of laser in powder bed. *Materials & Design*, *89*, 255–263.

Francis, B. A., & Wonham, W. M. (1975). The internal model principle for linear multivariable regulators. *Applied Mathematics and Optimization*, *2*(2), 170–194.

Hara, S., Yamamoto, Y., Omata, T., & Nakano, M. (1988). Repetitive control system: A new type servo system for periodic exogenous signals. *IEEE Transactions on Automatic Control*, *33*(7), 659–668.

He, X., Guo, D., & Leang, K. K. (2017). Repetitive control design and implementation for periodic motion tracking in aerial robots. In *American control conference, 2017* (pp. 5101–5108). IEEE.

Heralić, A., Christiansson, A.-K., & Lennartson, B. (2012). Height control of laser metal-wire deposition based on iterative learning control and 3D scanning. *Optics and Lasers in Engineering*, *50*(9), 1230–1241.

Hoelzle, D. J., & Barton, K. L. (2016). On spatial iterative learning control via 2-D convolution: Stability analysis and computational efficiency. *IEEE Transactions on Control Systems Technology*, *24*(4), 1504–1512.

Hofman, J., Pathiraj, B., Van Dijk, J., de Lange, D., & Meijer, J. (2012). A camera based feedback control strategy for the laser cladding process. *Journal of Materials Processing Technology*, *212*(11), 2455–2462.

Inoue, T., Nakano, M., Kubo, T., Matsumoto, S., & Baba, H. (1981). High accuracy control of a proton synchrotron magnet power supply. *IFAC Proceedings Volumes*, *14*(2), 3137–3142.

Jung, W. G. (2005). *Op Amp applications handbook*. Newnes.

Kannatey-Asibu Jr., E. (2009). *Principles of laser materials processing, Vol. 4*. John Wiley & Sons.

Kruth, J.-P., Froyen, L., Van Vaerenbergh, J., Mercelis, P., Rombouts, M., & Lauwers, B. (2004). Selective laser melting of iron-based powder. *Journal of Materials Processing Technology*, *149*(1), 616–622.

Kurniawan, E., Cao, Z., & Man, Z. (2011). Adaptive repetitive control of system subject to periodic disturbance with time-varying frequency. In *Informatics and computational intelligence, ICI, 2011 First international conference on* (pp. 185–190). IEEE.

Labudovic, M., Hu, D., & Kovacevic, R. (2003). A three dimensional model for direct laser metal powder deposition and rapid prototyping. *Journal of Materials Science*, *38*(1), 35–49.

Lim, I., Hoelzle, D. J., & Barton, K. L. (2017). A multi-objective iterative learning control approach for additive manufacturing applications. *Control Engineering Practice*, *64*, 74–87.

Liu, T., Wang, D., & Zhou, K. (2016). High-performance grid simulator using parallel structure fractional repetitive control. *IEEE Transactions on Power Electronics*, *31*(3), 2669–2679.

Liu, Z., Zhang, B., & Zhou, K. (2017). Universal fractional-order design of linear phase lead compensation multirate repetitive control for pwm inverters. *IEEE Transactions on Industrial Electronics*, *64*(9), 7132–7140.

Meng, W., Xie, S. Q., Liu, Q., Lu, C. Z., & Ai, Q. (2017). Robust iterative feedback tuning control of a compliant rehabilitation robot for repetitive ankle training. *IEEE/ASME Transactions on Mechatronics*, *22*(1), 173–184.

Merry, R. J., Kessels, D., Heemels, W., Van De Molengraft, M., & Steinbuch, M. (2011). Delay-varying repetitive control with application to a walking piezo actuator. *Automatica*, *47*(8), 1737–1743.

Nakano, M., She, J.-H., Mastuo, Y., & Hino, T. (1996). Elimination of position-dependent disturbances in constant-speed-rotation control systems. *Control Engineering Practice*, *4*(9), 1241–1248.

Navalkar, S., Van Wingerden, J., Van Solingen, E., Oomen, T., Pasterkamp, E., & Van Kuik, G. (2014). Subspace predictive repetitive control to mitigate periodic loads on large scale wind turbines. *Mechatronics*, *24*(8), 916–925.

Nazir, R., Zhou, K., Watson, N., & Wood, A. (2015). Analysis and synthesis of fractional order repetitive control for power converters. *Electric Power Systems Research*, *124*, 110–119.

Peyre, P., Aubry, P., Fabbro, R., Neveu, R., & Longuet, A. (2008). Analytical and numerical modelling of the direct metal deposition laser process. *Journal of Physics D: Applied Physics*, *41*(2), 025403.

Ramos, G. A., & Costa-Castelló, R. (2012). Power factor correction and harmonic compensation using second-order odd-harmonic repetitive control. *IET Control Theory & Applications*, *6*(11), 1633–1644.

Schmidt, M., Merklein, M., Bourell, D., Dimitrov, D., Hausotte, T., Wegener, K., et al. (2017). Laser based additive manufacturing in industry and academia. *CIRP Annals-Manufacturing Technology*, *66*(2), 561–583.

Simchi, A., & Pohl, H. (2003). Effects of laser sintering processing parameters on the microstructure and densification of iron powder. *Materials Science & Engineering A (Structural Materials: Properties, Microstructure and Processing)*, *359*(1), 119–128.

Steinbuch, M., Weiland, S., & Singh, T. (2007). Design of noise and period-time robust high-order repetitive control, with application to optical storage. *Automatica*, *43*(12), 2086–2095.

Wang, D., & Chen, X. (2017). A tutorial on loop-shaping control methodologies for precision positioning systems. *Advances in Mechanical Engineering*, *9*(12), 1687814017742824.

Wang, D., & Chen, X. (2018). A multirate repetitive control for fractional-order servos in laser-based additive manufacturing. In *American control conference, 2018*. IEEE (in production).

Yao, W.-S., Tsai, M.-C., & Yamamoto, Y. (2013). Implementation of repetitive controller for rejection of position-based periodic disturbances. *Control Engineering Practice*, *21*(9), 1226–1237.

Zou, Z.-X., Zhou, K., Wang, Z., & Cheng, M. (2015). Frequency-adaptive fractional-order repetitive control of shunt active power filters. *IEEE Transactions on Industrial Electronics*, *62*(3), 1659–1668.